



# Micro-Mechanical Fracture Investigations on Grain Size Tailored Tungsten-Copper Nanocomposites

K. SCHMUCK <sup>1,3</sup> M. BURTSCHER,<sup>1</sup> M. ALFREIDER,<sup>1</sup>  
M. WURMSHUBER,<sup>2</sup> and D. KIENER<sup>1</sup>

1.—Department of Material Science, Montanuniversität Leoben, Jahnstraße 12, 8700 Leoben, Styria, Austria. 2.—Department of Materials Science and Engineering, Friedrich-Alexander-University of Erlangen-Nürnberg, Martensstraße 5, 91058 Erlangen, Bavaria, Germany. 3.—e-mail: klemens.schmuck@unileoben.ac.at

Tungsten-copper composites are used in harsh environments because of their superior material properties. This work addresses a tungsten-copper composite made of 20 wt.% copper, which was subjected to grain refinement by high-pressure torsion, whereby the deformation temperature was varied between room temperature and 400 °C to tailor the grain size. Deformation was performed up to microstructural saturation and verified by hardness measurement and scanning electron microscopy. From the refined nanostructured material, micro-cantilever bending beams with cross-sections spanning from  $5 \times 5$  to  $35 \times 35 \mu\text{m}^2$  were cut to examine possible size effects and the grain size influence on the fracture behavior. Fracture experiments were performed in situ inside a scanning electron microscope by applying a quasi-static loading protocol with partial unloading steps. Inspection of the fracture surfaces showed that all cantilevers failed in an inter-crystalline fashion. Nevertheless, remaining coarser tungsten grains impacted the resultant fracture toughness and morphology. Cantilevers fabricated from the 400 °C specimen exhibited a fracture toughness of  $220 \pm 50 \frac{\text{J}}{\text{m}^2}$ . For the room temperature cantilevers, a fracture toughness of  $410 \pm 50 \frac{\text{J}}{\text{m}^2}$  was observed, which declined to  $340 \pm 30 \frac{\text{J}}{\text{m}^2}$  for cantilevers  $< 10 \times 10 \mu\text{m}^2$ , confirming a size effect. The increased fracture toughness is attributed to the delamination-like structures formed in the room temperature sample.

## INTRODUCTION

Materials with outstanding properties are required for high-performance applications and harsh environments, e.g., plasma-facing components in fusion reactors. For that purpose, tungsten and tungsten-based materials are frequently considered as candidate materials for structural and shielding components in fusion reactors because of the superior material properties of tungsten, such as high sputter resistance, low tritium retention in fusion environments, low vapor pressure, high melting point and good intrinsic strength at elevated temperatures.<sup>1–7</sup> Nevertheless, the use of

pure tungsten in safety-relevant applications is limited because of its low ductility and inherent brittle behavior, leading to a low overall damage tolerance.<sup>8,9</sup> Besides that, heat sinks used in fusion reactors to cool structural and shielding components are commonly fabricated from copper and copper-based alloys.<sup>7</sup> The thermal expansion coefficient between tungsten and copper differs, leading to high thermally induced stresses at their interfaces during high temperature loads. By fabricating tungsten-copper composites, the thermal stresses can be alleviated.<sup>4,10</sup> In addition, the secondary ductile copper phase enhances ductility of the composite, but degrades the intrinsic strength, whereby the extent depends on the material composition.<sup>11</sup> Strength and ductility must be enhanced to improve the damage tolerance.<sup>12,13</sup> A well-known method to increase strength and ductility

(Received October 10, 2023; accepted December 14, 2023; published online January 9, 2024)

simultaneously is grain refinement.<sup>14–16</sup> Coarse grained tungsten-copper composites with a copper content of 25 at.%, 51 at.% and 59 at.% have been successfully subjected to high-pressure torsion for grain refinement down to the nanocrystalline regime. For all compositions the microstructure, hardness and resulting grain size in saturation were analyzed, connecting deformation temperature with the saturated grain size.<sup>17–20</sup> While the structural evolution is well documented, the fracture mechanical behavior was so far only investigated for the nanocrystalline tungsten-copper composition with 59 at.% copper using micro-cantilever bending experiments,<sup>20</sup> preventing a detailed understanding of the influence of the grain size on the fracture toughness.

To contribute to this lack of knowledge, in this work a tungsten-copper composite with a copper content of only 42 at.% was subjected to high-pressure torsion at different deformation temperatures to tailor the nanocrystalline grain size. The sample disks were deformed up to the saturation regime to avoid microstructural gradients along the radius. Subsequently, micro-cantilever bending beams were fabricated from these disks to investigate the fracture toughness for different nanocrystalline grain sizes.

## EXPERIMENTAL

### Sample Preparation

The base material was a liquid phase sintered tungsten-copper composite rod with a copper content of 42 at.% (20 wt.%) and a mean tungsten grain size of  $2.5 \mu\text{m}$  (WHS Sondermetalle, Grünsfeld, Germany). From this rod with a diameter of 8 mm, three disks with a thickness of roughly 1 mm were cut. Subsequently, the disks were subjected to high-pressure torsion (HPT<sup>21</sup>) at deformation temperatures of room temperature (RT), 200 °C and 400 °C to tailor the resultant grain size. To obtain a saturated microstructure, an equivalent strain of 160 and 680 according to Pippan et al.<sup>21</sup> was applied

at a radius of 3 mm for the RT and the two elevated temperatures samples, respectively.

After HPT, the samples were cut into halves along the transversal plane with a wire saw, depicted in Fig. 1a. One half was embedded and polished to verify the saturated and homogeneous microstructure along the radius. For quantitative verification of the saturation level, Vickers hardness measurements (HV1, Buehler Micromet 5104) were performed along the radius. The indents were placed 0.25 mm apart from each other, schematically shown by the diamond shapes in Fig. 1a. Furthermore, saturation and homogeneity of the microstructure were qualitatively investigated by scanning electron microscopy (SEM; Zeiss LEO type 1525) along the radius every 0.5 mm; see the exemplary blue rectangles in Fig. 1a.

The second half disk was further cut into pieces. Along one quarter the matrix grain size was quantitatively investigated by scanning transmission electron microscopy (STEM; JEOL JEM-2200FS microscope, JEOL Ltd., Japan). To reduce preparation time, the specimen was manually ground and polished to a wedge-like shape exhibiting a final thickness of about  $20 \mu\text{m}$  at the wedge tip. After manual polishing, focused ion beam milling (FIB; Zeiss Auriga Laser platform, Carl Zeiss AG, Oberkochen, Germany) was used to mill thin lamellas; thereby, the FIB current was subsequently reduced from 20 nA, for coarse milling, to 50 pA for polishing. The final thickness of the lamellas was about 100 nm with an area of about  $2 \times 5 \mu\text{m}^2$  to investigate the nanocrystalline grain size, which was analyzed with image processing techniques using grain segmentation by the watershed algorithm.<sup>20,22</sup>

The other quarter of the HPT disk was used to fabricate differently sized micro-cantilever bending beams. For that the piece was manually ground and polished to a wedge shape with a final thickness between 20 and  $50 \mu\text{m}$ . To further reduce the FIB time, femtosecond laser ablation<sup>23</sup> within an FIB/SEM (Zeiss Auriga Laser platform, Carl Zeiss AG,

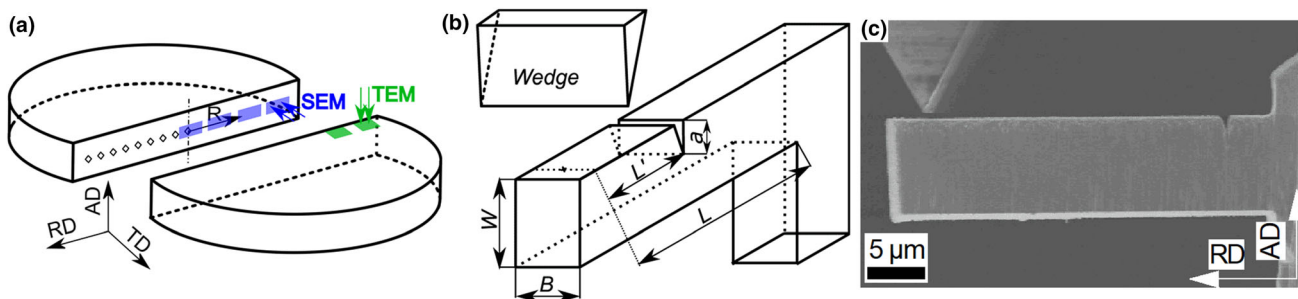


Fig. 1. Sample preparation and testing. (a) Compacted disk after high-pressure torsion processing. The disk is shown in halves to enhance visibility. The colors blue and green represent SEM and TEM measurements, respectively. The arrows depict the viewing direction, while the surface normal to the viewing direction was polished. The coordinate system defines the radial (RD), axial (AD) and tangential direction (TD). (b) Schematic sketch of the cantilever dimensions, with  $W \times B$  the cantilever cross-section,  $a$  the crack length,  $L'$  the length between indenter and crack and  $L$  the length between indenter loading point and fixation. (c) Fabricated cantilever before *in situ* testing and relation to the HPT disk orientation (Color figure online).

Oberkochen, Germany) was performed for coarse machining and pre-cutting of the cantilevers. Final processing was done via FIB milling by subsequently reducing the FIB current from 20 nA for coarse milling to 500 pA for polishing. For the RT sample, the cantilever cross-sections were varied between  $5 \times 5$  and  $35 \times 35 \mu\text{m}^2$  to investigate a possible size effect on initiation fracture toughness ( $J_q$ ). For the 400 °C sample, only cantilevers with cross-sections of  $5 \times 5$  and  $10 \times 10 \mu\text{m}^2$  were fabricated. The cantilever length was set to about  $4W$  and the initial notch depth between  $(0.3 - 0.4)W$ . The notches were introduced by line milling from the top view with a current of 500 pA. To reach the desired depth for the largest cantilevers of  $35 \times 35 \mu\text{m}^2$ , the notch was pre-cut from the side view and finished in the top view, respectively. The cantilever geometry and important variables are schematically illustrated in Fig. 1b, while the in situ setup is shown in Fig. 1c.

### Testing Setup

Fracture experiments were performed inside an SEM (DSM 982, Carl Zeiss AG, Oberkochen, Germany), which allowed to record in situ images at a rate of one image per second using an in-lens secondary electron detector. The imaged region was selected to the crack vicinity to enhance image resolution at the crack tip. The cantilevers were loaded with a displacement controlled micro indenter (UNAT SEM 1, ASMEC GmbH, Dresden, Germany) with a noise level of  $50 \mu\text{N}$  in vacuum. Loading was performed quasi-statically with up to 15 evenly spaced sequential unloading steps.<sup>24</sup> Each loading/unloading step consists of the following segments: loading with a constant displacement rate of 50 nm/s, holding for 10 s, unloading with a displacement drop of 10% capped at  $2 \mu\text{m}$  and holding again for 10 s. Due to the cross-sectional variation of the cantilevers, the maximal displacement was set to  $26 \mu\text{m}$  for the cross-sections of  $35 \times 35$  and  $20 \times 20 \mu\text{m}^2$ , to  $16 \mu\text{m}$  for the  $10 \times 10 \mu\text{m}^2$  cantilever and to  $8 \mu\text{m}$  for the  $7.5 \times 7.5$  and  $5 \times 5 \mu\text{m}^2$  cantilevers, respectively.

### Fracture Mechanical Evaluation

The fracture characteristics of the cantilevers were determined from the recorded load-displacement data by relating stiffness changes to cross-sectional variation with respect to the crack length.<sup>25</sup> The cantilever stiffness was measured by linearly fitting the unloading segment for each loading cycle.<sup>24</sup> The first unloading stiffness in combination with the initial crack length, measured before the experiment, was used as a reference to relate stiffness changes to crack growth, according to Ref. 25. Furthermore, the  $J$ -integral was calculated employing elastic-plastic fracture mechanics (EPFM) following the detailed description outlined by Alfreider et al.,<sup>26</sup> as all cantilevers showed

noticeable non-linearity before fracture; see the representative loading curves in Fig. 2.

To compare the obtained  $J_q$  to data from literature and linear elastic fracture mechanics, the  $J_q$  values were transformed into fracture toughness ( $K_q$ ) using in linear-elastic fracture mechanics according to the ASTM1820 standard<sup>27</sup> by:

$$K_q = \sqrt{\frac{J_q E}{(1-\nu^2)}}, \quad (1)$$

with the Young's modulus  $E = 221 \text{ GPa}$ , measured by nanoindentation and the Poisson ratio  $\nu = 0.32$ .<sup>28</sup>

Besides the  $J$ -integral, the crack tip opening displacement ( $\delta$ ) is frequently used in EPFM to characterize failure processes. This can be measured from the recorded in situ frames; therefore, for stable crack growth, the last frame before crack initiation was used, while in the case of unstable crack growth the frame before fracture was analyzed. Measurement of  $\delta$  was performed manually as described by Shih et al.,<sup>29</sup> where two orthogonal lines are placed on the crack tip, so that the distance between the crack tip and the intersection with the crack flanks are equal for both lines.  $\delta$  is then given by the distance between the crack flank intersection points. This is shown in

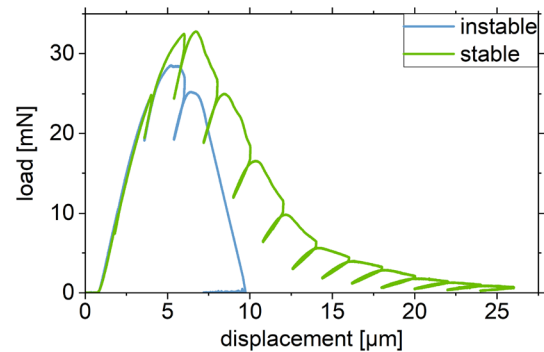


Fig. 2. Representative load-displacement data recorded for stable and unstable fracture, respectively, revealing in both cases a noticeable non-linearity before fracture.

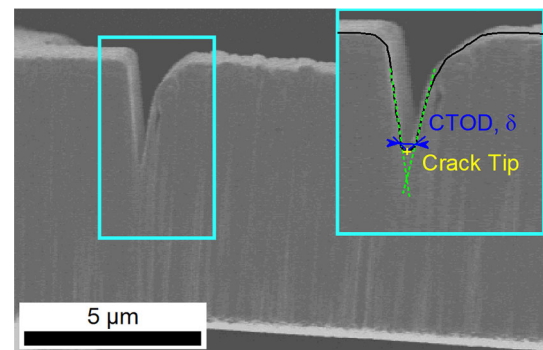


Fig. 3. Manual  $\delta$  measurement example on an in situ recorded micrograph. Note that the inset, marked with cyan, is distorted in  $x$ -direction for visualization reasons. The yellow cross represents the crack tip, while the green dashed lines fit the crack flank (Color figure online).

Fig. 3. For EPFM it has been shown that both parameters  $J_q$  and  $\delta$  are linked via:

$$\delta = d_n \frac{J_q}{\sigma_y}, \quad (2)$$

with  $\sigma_y$  being the materials yield strength and  $d_n$  the Shih factor depending on the stress condition and hardening behavior of the material.<sup>29</sup>

## RESULTS

### Microstructural Investigations

Vickers hardness measurements were performed for all specimens to verify microstructural saturation along the disk radius, as the hardness is inversely proportional to the grain size according to the Hall-Petch relation.<sup>14–16</sup> The hardness values measured are depicted in Fig. 4 for all samples, whereby the mean hardness values above a radius of 1.5 mm in the saturation regime are  $6.8 \pm 0.2$ ,  $6.7 \pm 0.2$  and  $6.2 \pm 0.1$  GPa for the RT, 200 °C and 400 °C sample, respectively.

Furthermore, the microstructure was examined by backscatter electron imaging along the radius. The microstructures at a radius of 3 mm are depicted in Fig. 5a, b and c as representative microstructures above a radius of 1.5 mm for the HPT deformation temperature of RT, 200 °C and 400 °C, respectively. Despite the verified saturation by Vickers hardness measurements, the microstructures showed a bi-modal grain size characteristic with statistically distributed coarse tungsten grains embedded in a nanocrystalline matrix of copper and tungsten. Bright regions in the microstructure represent coarse tungsten grains; see Fig. 5a-c. With increasing deformation temperature, the coarse tungsten grains change their shape from an elongated flake-like, lamellar form to a spherical shape at 200 °C and 400 °C; compare Fig. 5a-c. Thereby, the median equivalent Feret diameter of the coarse tungsten grains increased from 200 to 233 nm between the RT and 400 °C.

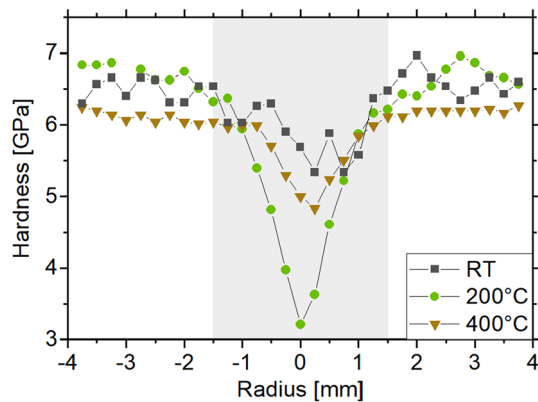


Fig. 4. Vickers hardness measurement along the radius of the samples fabricated via HPT deformation at RT, 200 °C and 400 °C, respectively. The gray shaded area encloses the region with insufficient straining and thus unsaturated microstructure.

Furthermore, the nanocrystalline matrix was investigated by STEM at a radius of about 3 mm. These investigations revealed an increasing grain size trend of the nanocrystalline matrix with rising deformation temperature; see Fig. 5d-f. For the specimens deformed at elevated temperatures, a few coarse tungsten grains are present in the STEM images, while for the RT specimen none are evident. This arises from the flake-like structure in the RT specimen, which is oriented parallel to the lamella and thinner than the spherical grains observed in the elevated temperature specimens. Hence, the probability of capturing these flake-like structures in this TEM lamella orientation is reduced. For proper statistics, at least four images were analyzed for each deformation temperature to quantify the matrix grain size. The resulting grain size distributions are depicted in Fig. 6, while the central statistical values are listed in Table I.

### Fracture Mechanical Testing

Notched micro-cantilever bending beams were cut to examine the fracture behavior of the RT and 400 °C sample. The cantilevers were fabricated in pairs and grouped by size at a disk radius between 2 and 3.5 mm. Furthermore, they were orientated along the radial direction, with the notch being parallel to the axial direction; see Fig. 1a and c for reference. Hence, the coarse flake-like tungsten grains evident in the RT specimen are parallel to the cantilever. For the RT specimen, the cantilever cross-section was varied between  $5 \times 5$  and  $35 \times 35 \mu\text{m}^2$  to investigate a possible sample size effect. Thereby, the initial crack length  $a_0$  was measured for the individual cantilever sizes as:  $2.4 \pm 0.5 \mu\text{m}$  ( $\frac{a_0}{W} = 37 \pm 7\%$ ),  $2.3 \pm 0.3 \mu\text{m}$  ( $\frac{a_0}{W} = 31 \pm 2\%$ ),  $3.4 \pm 0.7 \mu\text{m}$  ( $\frac{a_0}{W} = 33 \pm 8\%$ ),  $5.8 \pm 0.7 \mu\text{m}$  ( $\frac{a_0}{W} = 29 \pm 4\%$ ) and  $15.9 \pm 0.8 \mu\text{m}$  ( $\frac{a_0}{W} = 46 \pm 2\%$ ), for the  $5 \times 5$ ,  $7.5 \times 7.5$ ,  $10 \times 10$ ,  $20 \times 20$  and  $35 \times 35 \mu\text{m}^2$  cantilever, respectively. Despite the cross-sectional variation, the cantilevers from the RT sample fractured primarily by stable crack growth. Fig. 7Ia-Ij depicts representative fracture surfaces for the different cantilever sizes of the RT sample. The subfigures Ia-Id and If show failure by stable crack growth, while subfigure Ie illustrates a fracture surface after unstable failure. Furthermore, to investigate a grain size dependency of the fracture toughness, cantilevers with a cross-section of  $5 \times 5$  and  $10 \times 10 \mu\text{m}^2$  were fabricated from the 400 °C sample. For these cantilevers, an initial crack length  $a_0$  was determined to  $2.1 \pm 0.3 \mu\text{m}$  ( $\frac{a_0}{W} = 36 \pm 4\%$ ) and  $3.8 \pm 0.4 \mu\text{m}$  ( $\frac{a_0}{W} = 36 \pm 4\%$ ) for the  $5 \times 5$  and  $10 \times 10 \mu\text{m}^2$  cantilevers, respectively. For the 400 °C sample, all cantilevers with a cross-section of  $5 \times 5 \mu\text{m}^2$  showed stable crack growth, while all having a cross-section of  $10 \times 10 \mu\text{m}^2$  fractured unstably. The fracture surfaces for the 400 °C cantilevers are displayed in Fig. 7IIa and IIb.

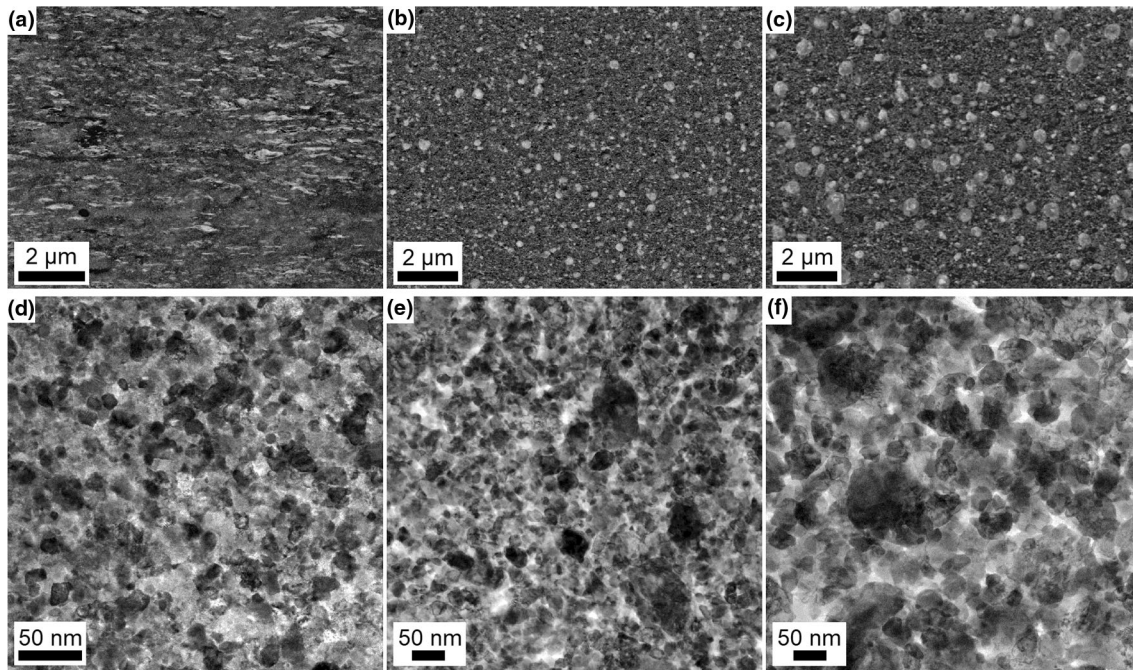


Fig. 5. Obtained microstructures for the different deformation temperatures at a disk radius of 3 mm. (a)-(c) Backscatter electron images for deformation at (a) RT, (b) 200 °C and (c) 400 °C. The bright spots represent coarse tungsten grains. (d)-(f) STEM investigations of the nanocrystalline matrix for deformation temperatures of (d) RT, (e) 200 °C and (f) 400 °C.

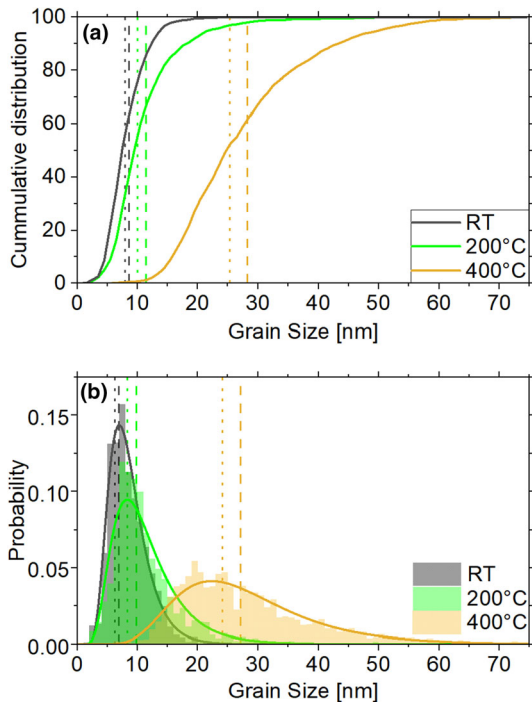


Fig. 6. Matrix grain size distribution measured at a radius of 3 mm for the samples deformed at RT, 200 °C and 400 °C. (a) Cumulative and (b) probability distribution. The dashed lines represent the mean values, while the dotted ones correspond to the median values.

All load-displacement curves showed noticeable non-linearity before crack initiation or catastrophic failure; see the representative Fig. 2. Hence, EPFM was used to characterize the fracture process of all

**Table I. Central values of the matrix grain size distribution in nm, where p15 and p85 represent the 15% and 85% percentile**

T (°C)	Mean	Median	p15	p85	Grains
RT	9	8	5	12	1658
200	11	10	6	17	1777
400	28	26	17	39	1758

cantilevers. For stable crack growth, the  $J_q$  was determined before crack initiation, whereby intermediate values between two unloading steps were linearly interpolated. Thereby, the crack growth initiation was determined by visually inspecting the in situ frames for some crack extension, neglecting crack tip blunting. The  $J_q$  was obtained at the initiation as the transition between blunting and tearing regime becomes harder to distinguish with decreasing cantilever size, making fitting of either regime challenging; see Fig. 8. This occurs because the tearing modulus is indirectly proportional to the sample size.<sup>30</sup>

For stable crack growth, the uncertainty was approximated by  $\frac{J_{n+1}-J_n}{2}$ . For unstable crack growth,  $J_q$  was determined at the maximum load, including the load-displacement area between the last unloading step before failure and maximum load, as schematically illustrated in Fig. 8. To validate the  $J_q$  values, the validation criterion

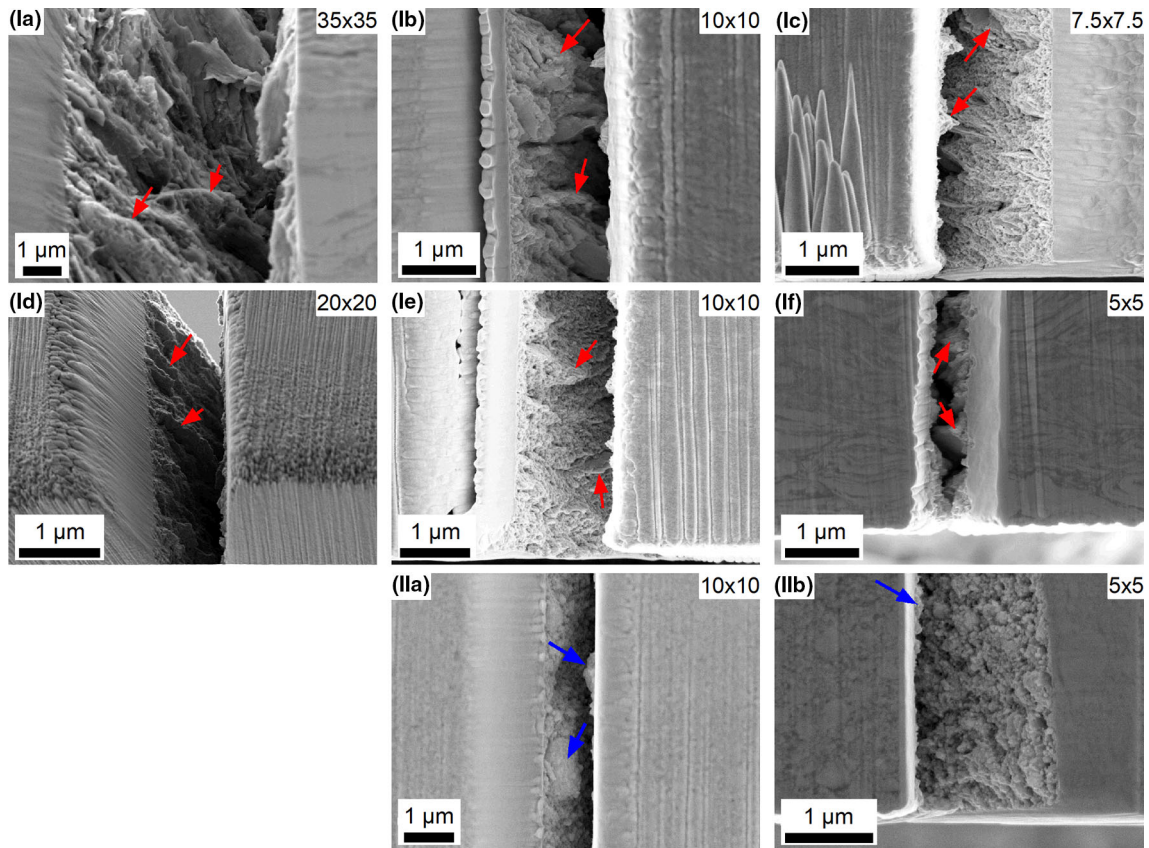


Fig. 7. Postmortem fracture surfaces for the different cantilever sizes fabricated from the RT sample in (Ia)-(Ic) and the 400 °C sample in (IIa)-(IIb). Images (Ia)-(Id), (Ie) and (IIb) illustrate fracture surfaces after stable crack growth, while the surfaces shown in (Ie) and (IIa) represent unstable fracture. The red arrows indicate coarse tungsten grains, which form delamination-like structures for the RT sample, and the blue arrows point to the spherical-shaped coarse tungsten grains in the 400 °C sample (Color figure online).

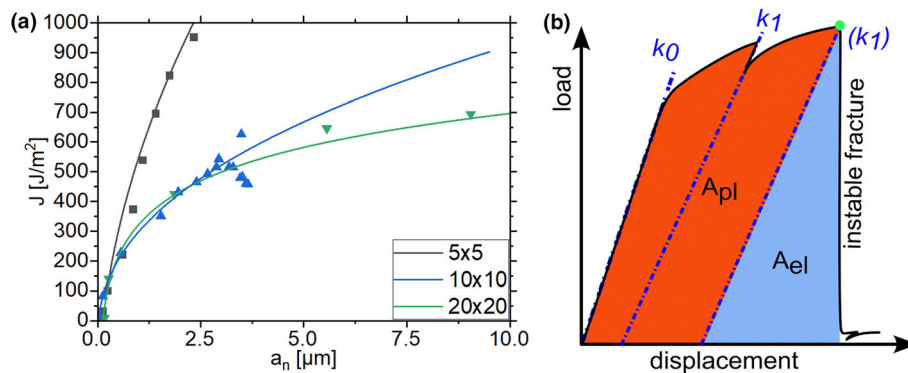


Fig. 8. (a) Representative R-curves fitted by a power-law fit for cantilever dimensions of  $5 \times 5$ ,  $10 \times 10$  and  $20 \times 20 \mu\text{m}^2$ , showing an increasing tearing modulus with decreasing size, rendering distinguishing between blunting and tearing part a challenging task. (b) Schematic illustration for the evaluation of  $J_q$  for unstable fracture, with  $k_n$  the unloading stiffness,  $A_{pl}$  the plastic area and  $A_{el}$  the elastic area. Thereby,  $J_q$  is evaluated at the maximum load (green dot), and the area below the load-displacement curve is split into plastic and elastic area according to the last unloading stiffness ( $k_1$ ) (Color figure online).

$$\{(W - a_0); B\} > C \frac{J_q}{\sigma_y}, \quad (3)$$

is frequently used in EPFM, where  $C$  is a pre-factor ranging between 10 and 50,<sup>24,29,31-33</sup> whereby the ASTM1820 standard states a value of 10.<sup>27</sup>

The  $J_q$  values determined for all RT cantilevers are shown in Fig. 9a. Thereby, the  $C$  parameter is

calculated from Eq. 3 by taking the minimum of the left side and solving the equation for  $C$  by assuming an equal sign. Among similar cantilever dimensions for the RT sample, median  $J_q$  values of  $340 \pm 30$ ,  $370 \pm 40$ ,  $400 \pm 90$ ,  $420 \pm 50$  and  $410 \pm 30 \frac{\text{J}}{\text{m}^2}$  were determined for the cantilever cross-section  $5 \times 5$ ,

7.5 × 7.5, 10 × 10, 20 × 20 and 35 × 35 μm<sup>2</sup>, respectively.

In addition, the δ was determined, which was challenging, as image resolution is limited because of the necessity of imaging the total cantilever height and image noise present due to the fast frame acquisition required to capture the fracture process. Thus, δ was measured several times and averaged to obtain an accurate value. For comparison, the δ values were transformed according to Eq. 2 using a Shih factor of 0.78 for a non-hardening material and the plane strain condition.<sup>29</sup> The yield strength was approximated from the hardness measurements by  $\sigma_y \approx \frac{9.810665}{3} HV$ ,<sup>34</sup> which gives 2250 ± 60 MPa, 2330 ± 70 MPa and 2050 ± 30 MPa for the RT, 200 °C and 400 °C sample, respectively. Fig. 9b depicts the measured and transformed δ values for the RT sample, whereby values of 125 ± 7, 129 ± 6, 143 ± 6, 146 ± 7 and 152 ± 3 nm were found for the cantilever cross-sections of 5 × 5, 7.5 × 7.5, 10 × 10, 20 × 20 and 35 × 35 μm<sup>2</sup>, respectively. This translates to  $J_{q,\delta}$  values of 360 ± 20, 370 ± 20, 400 ± 20, 410 ± 20 and

430 ± 20  $\frac{J}{m^2}$  for these dimensions of the RT sample, respectively.

The  $J_q$  determined from mechanical data for the cantilevers fabricated from the 400 °C sample are depicted in Fig. 10a. Additionally, the  $J_q$  values of the RT cantilevers with varying cross-section are displayed for a direct comparison. Cantilevers with a cross-section of 10 × 10 μm<sup>2</sup> from the 400 °C sample exhibited a  $J_q$  of 220 ± 60  $\frac{J}{m^2}$ , while cantilevers with a cross-section of 5 × 5 μm<sup>2</sup> gave 230 ± 40  $\frac{J}{m^2}$ . Furthermore, δ values were measured from the in situ frames for the 400 °C cantilevers and are illustrated in Fig. 10b. Additionally, the δ data from the various RT cantilevers are included for a direct comparison. The 400 °C cantilevers exhibited a δ of 90 ± 6 and 91 ± 6 nm, which gives a  $J_{q,\delta}$  value of 230 ± 20 and 240 ± 20  $\frac{J}{m^2}$  for the cantilever cross-sections 5 × 5 and 10 × 10 μm<sup>2</sup>, respectively.

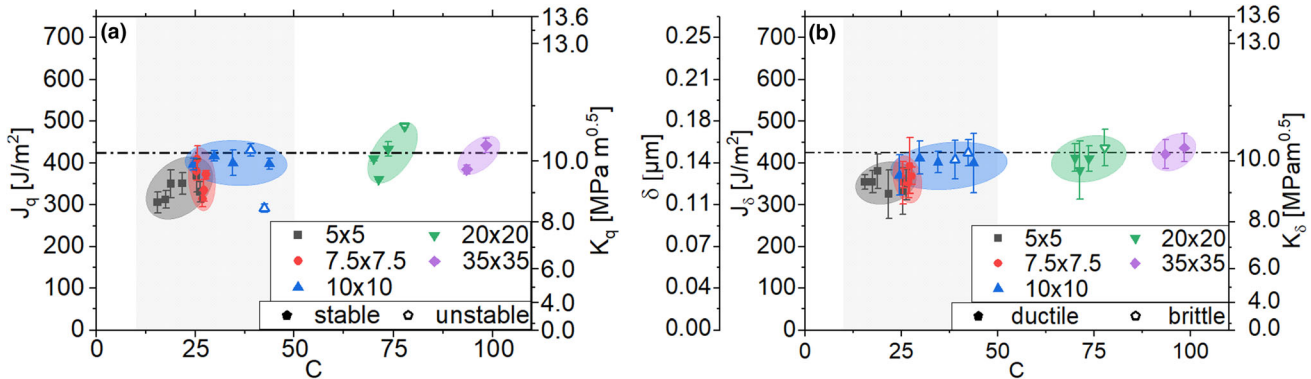


Fig. 9. Characteristic fracture values depending on the pre-factor  $C$  given in Eq. 3. The gray shaded area represents the minimum validity region of the  $J$ -integral for EPFM from the literature.<sup>24,27,29,31–33</sup> The horizontal line indicates the size-independent fracture toughness  $J_q$  obtained from the larger cantilevers. (a)  $J_q$  values from the R-curve determined from the load-displacement data of RT sample. (b) Measured values of the  $\delta$  before crack growth initiation or failure converted into fracture toughness  $J_q$  according to Eq. 2.

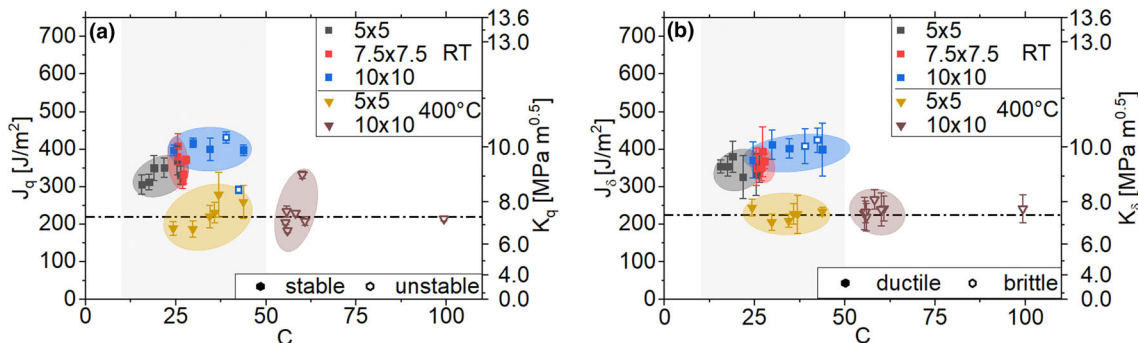


Fig. 10. Comparison of the fracture characteristics between the RT and 400 °C deformed samples. The fracture toughness  $J_q$  is plotted over the pre-factor  $C$  given in Eq. 3, while the gray shaded region illustrates the minimum validity criterion range for the  $J$ -integral in EPFM according to literature.<sup>24,27,29,31–33</sup> (a) Fracture toughness values  $J_q$  obtained from the R-curve, which was calculated from mechanical data. (b)  $\delta$  values before failure or crack growth initiation, transformed into fracture toughness values according to Eq. 2.

## DISCUSSION

### Microstructural Investigations

The equivalent strain, introduced via HPT, depends linearly on the radius. Hence, with increasing radius more strain is introduced into the sample upon deformation, leading to an increased refinement of the microstructure. Exceeding the radius of 1.5 mm, the hardness converges to a constant value, indicating microstructural saturation; see Fig. 4. Comparing the hardness among the different deformation temperatures, similar values for the sample deformed at RT and 200 °C are evident, while the 400 °C sample shows a slightly decreased hardness, in agreement with an increased grain size, as depicted in Fig. 6. This indicates being still within the Hall-Petch regime.<sup>35,36</sup> The hardness values are comparable to literature data of a bulk tungsten-copper composite with 59 at.% (33 wt.%) copper deformed at RT to the nanocrystalline regime, where a final hardness from 6 to 8 GPa was reached.<sup>19</sup> Nevertheless, Vickers hardness measurements examine the whole imprint volume at once, allowing to detect only mean changes within the imprint size. Hence, additional SEM investigations were performed, revealing a similar trend as the hardness values. No significant differences were observable in the microstructure above a radius of 1.5 mm, verifying microstructural saturation. Nevertheless, the observed microstructures show a bimodal structure, consisting of statistically comparably distributed coarse tungsten grains, with an equivalent diameter of hundreds of nm, embedded into a truly nanocrystalline matrix; see Fig. 5a-c. This occurs as the deformation is mainly localized in the softer copper phase, and the volume fraction of the nanocrystalline matrix increases during deformation, limiting the contact between large tungsten particles.<sup>18</sup> With increasing deformation temperature, the copper phase softens because of the related increase in homologous temperature from 0.22 to 0.35 and 0.5, respectively.<sup>37</sup> This leads to less grain refinement and a more spherical shape for the present coarse tungsten grains in the samples deformed at elevated temperatures, as illustrated in Fig. 5a-c.

From STEM images of the nanocrystalline matrix, an increasing grain size with increased deformation temperature is obvious; see Fig. 5d-f. The quantitative analysis of the nanocrystalline matrix by STEM, listed in Table I, revealed a similar mean grain size of about 10 nm for the RT and 200 °C samples. At the same time, the distribution slightly broadens from RT to 200 °C, illustrated in Fig. 6. For the sample deformed at 400 °C, the mean grain size of the nanocrystalline matrix shifts to a significantly higher value of 28 nm and the grain size distribution broadens notably; see Fig. 6. Furthermore, the 400 °C sample displays only a minor overlap with the distributions of the other samples, as there are fewer small grains. The

grain size values determined for the RT sample are in accordance with literature data from HPT refined bulk tungsten-copper composites. For these, SEM investigations revealed a grain size range of 10 – 20 nm when containing 25 at.% (10 wt.%) copper,<sup>17</sup> while TEM investigations revealed a grain size range of 5 – 15 nm for 51 at.% (26 wt.%) copper.<sup>18</sup> For the elevated temperatures, 200 °C and 400 °C, the literature states a broader grain size range of 10 – 100 nm and 20 – 200 nm for a tungsten-copper-25 at.% composite,<sup>17</sup> measured by SEM. The mean grain size values determined in this study are on the lower end of the literature range.<sup>17,18</sup> This is not surprising, as in the present study nanocrystalline matrix was deliberately investigated by STEM, excluding the coarse tungsten grains present in the microstructure.

Besides, the HPT parameters used in this study to tailor the microstructure and grain size can be used as starting point for other material compositions. Nevertheless, additional investigations are necessary for new material compositions, as the deformation process in HPT is related to the material properties, e.g., the saturation grain size depends on the strength of the material. Schweiger et al.<sup>38</sup> reported a detailed insight into the different aspects of HPT deformation by using an iron-titanium-copper composite as model material. They concluded that for new multi-phase materials the interaction between the phases must be carefully examined to achieve a homogeneous structure by HPT.

### Fracture Mechanical Testing

Concerning the conducted miniaturized fracture experiments, all cantilevers were fabricated in the region of microstructural saturation, which was verified by hardness measurements and microstructural investigations; see Figs. 4 and 5. Nevertheless, coarse tungsten grains were still present in this region. These grains are statistically distributed and an order of magnitude smaller than the smallest cantilever size. Hence, these coarse tungsten grains are present in all cantilevers and are expected to have minor influence on the fracture behavior regarding the sample size. The fracture process of all cantilevers was governed by intercrystalline failure, evident by the small feature size of the rough surface structure regardless of cantilever dimensions and deformation temperatures; see Fig. 7. For the RT cantilevers, postmortem analysis of the fracture surface showed delamination-like structures, which have a similar extent as the coarse tungsten grains documented in the microstructure. This is depicted in Fig. 7Ia–If, where some delamination-like structures are marked by red arrows. Delaminations are known to transform the stress state at the crack front into a state with lower stress triaxiality (plane stress) by dividing the cross-section into smaller segments and improve the resulting fracture toughness of the



material.<sup>39,40</sup> Although the RT cantilevers mainly fractured in a stable manner, a few cantilevers exhibited unstable failure. By comparing the fracture surfaces of the stable and unstable fractured samples, it is noticeable that the fracture surface of the brittle cantilevers showed a slightly reduced number of delamination-like structures; compare Fig. 7Ib and Ie. Thus, for the unstable fracturing cantilevers, the stress triaxiality at the crack front is more pronounced compared to cantilevers exhibiting a stable crack growth. For the 400 °C sample, all cantilevers with a cross-section of  $10 \times 10 \mu\text{m}^2$  fractured unstably, while the cantilevers with a cross-section of  $5 \times 5 \mu\text{m}^2$  exhibited stable crack growth; see Fig. 10. Despite the different failure behaviors, both cantilever dimensions revealed a similar fracture surface, where the coarse tungsten grains are bypassed by the fracture path; see blue arrows in Fig. 7IIa and IIb. Fracture surface comparison of RT and 400 °C shows a rougher structure for the 400 °C samples; see Fig. 7IIa-IIb. This stems from the inter-crystalline fracture process and the increased matrix grain size, raised from 10 to 28 nm, as shown in Fig. 6. Furthermore, the coarse tungsten grains form delamination-like structures for the RT cantilevers, thereby lowering the stress triaxiality. In contrast, for the 400 °C specimens, the fracture path bypassed these grains, and coarse tungsten grains are pulled out from the other side; see Fig. 7IIa and IIb. Hence, the fracture toughness of the RT sample will be increased compared to the 400 °C cantilevers because of the reduced stress triaxiality, as depicted in Fig. 10.

The fracture toughness was quantified by EPFM, as all load-displacement curves showed noticeable non-linearity before crack growth; see Fig. 2. The RT cantilevers with cross-sections of  $20 \times 20$  and  $35 \times 35 \mu\text{m}^2$  were assessed to be above the most conservative pre-factor  $C$  in Eq. 3, which ranges from 10 to 50 for size independency in the literature.<sup>24,27,29,31-33</sup> For both cantilever dimensions, a similar  $J_q$  of about  $410 \pm 50 \frac{\text{J}}{\text{m}^2}$  was evaluated, assuring sample size independence for these cross-sections due to the relative size difference, depicted in Fig. 9a. The other cantilevers on the RT sample were dimensioned to be within the pre-factor  $C$  range of 10 to 50, resulting in cross-sectional sizes of  $5 \times 5$ ,  $7.5 \times 7.5$  and  $10 \times 10 \mu\text{m}^2$ . For these cantilevers, the determined  $J_q$  showed an increased scatter, originating from a decreasing fracture load with reduced cantilever size, therefore deteriorating the signal to noise ratio of the load sensor; see the  $J_q$  scatter in Fig. 9a. Additionally, the initial ligament impacts the determination of the plastic part from the  $J$ -integral.<sup>41</sup> The experimental ligament variations for the fabricated cantilevers are rather small, and therefore a significant impact on the determined  $J_q$  values is not expected. Nevertheless, the minor variations might contribute to the scatter of

the  $J_q$  values observed; see the increased scatter of the  $10 \times 10 \mu\text{m}^2$  cantilevers. However, the resultant  $J_q$  of  $400 \pm 90 \frac{\text{J}}{\text{m}^2}$  for the cantilever cross-section of  $10 \times 10 \mu\text{m}^2$  is similar to the value determined for the cantilevers with a cross-section of  $20 \times 20$  and  $35 \times 35 \mu\text{m}^2$ . This indicates size independency for the  $10 \times 10 \mu\text{m}^2$  cantilevers; see Fig. 9a. Conversely the cantilever with a cross-section of  $5 \times 5$  and  $7.5 \times 7.5 \mu\text{m}^2$  exhibited a slightly decreased  $J_q$  of  $340 \pm 30$  and  $370 \pm 40 \frac{\text{J}}{\text{m}^2}$ , pointing to a distinct sample size effect; see the declining  $J_q$  values below a pre-factor  $C < 30$  in Fig. 9a. A similar pre-factor value for sample size independency was reported by Wurmshuber et al.<sup>33</sup> for micro-cantilever bending beams fabricated from grain boundary-doped tungsten alloys with a grain size of about 150 nm. However, the application field of the investigated material is above the  $\mu\text{m}$  regime, where the sample size effect is expected. Nevertheless, future application might apply only to thin films of this material; hence, thorough investigations of the sample size effect are crucial.

Additionally,  $\delta$  was determined from the in situ frames, which directly relates to the plastic zone size on the surface ahead of the crack. Therefore, the  $\delta$  measurement is unaffected by the ligament variations. Cantilevers on the RT sample with a cross-section between  $10 \times 10$  and  $35 \times 35 \mu\text{m}^2$  showed a similar value of approximately  $146 \pm 7$  nm, illustrated in Fig. 9b. Conversion into  $J_{q,\delta}$  according to Eq. 2 gives a value of  $420 \pm 20 \frac{\text{J}}{\text{m}^2}$ , which is in excellent agreement with the  $J_q$  value of  $410 \frac{\text{J}}{\text{m}^2}$  obtained from mechanical data, ensuring size independence. The RT cantilevers with cross-sections of  $5 \times 5$  and  $7.5 \times 7.5 \mu\text{m}^2$  revealed a decreased  $\delta$  of  $125 \pm 7$  and  $129 \pm 6$  nm. Conversion to  $J_{q,\delta}$  gives values of  $360 \pm 20$  and  $370 \pm 20 \frac{\text{J}}{\text{m}^2}$  for these cantilevers, which are similar to  $J_q$  and exhibit the same trend of a decreasing  $J_q$ . The decline of both characteristic values signifies a sample size effect on the fracture toughness. The criteria given in Eq. 3 sets limits to the minimal cantilever thickness ( $B$ ) and the ligament length ( $W - a_0$ ) for sample size independency. The former defines the dominate stress state at the crack front to be plane strain, while the ligament length in conjunction with the plastic zone size defines the valid fracture model, whether the fracture is governed by small-scale, large-scale yielding or plastic collapse.<sup>33,42</sup> Besides the criteria given in Eq. 3,  $\delta$  can be used to define a sample size independency criteria, which is given by:<sup>42</sup>

$$W - a_0, B > 10\delta. \quad (4)$$

This criterion suggests a minimal cantilever thickness and ligament length of approximately  $1.5 \mu\text{m}$ . In this case  $B$ , this is fulfilled by all RT cantilevers, maintaining the plane strain condition. Therefore, the initiation parameters should be

constant over the different cantilever dimensions regarding the thickness.<sup>42</sup> Furthermore, the ligament length of all RT cantilevers is above the criteria given in Eq. 4, and analysis of the frames recorded in situ showed no significant plastic deformation, excluding the occurrence of plastic collapse. Nevertheless, a decline of the toughness values is evident with decreasing size, which might stem from stress gradients due to bending. The plastic zone size was estimated by the simple Irwin model, which is given for the plane strain condition as:

$$r_p = \frac{1}{6\pi} \left( \frac{K_q}{\sigma_y} \right)^2, \quad (5)$$

with  $r_p$  as the plastic zone radius.<sup>43,44</sup> In combination with Eq. 1 and the obtained values for  $J_q$  this gives an approximate  $r_p = 1.1 \pm 0.2 \mu\text{m}$  for the RT cantilevers. Furthermore, due to the bending applied to the cantilever, a strain gradient forms within the ligament, which gets steeper with decreasing sample dimensions. For cantilevers with a cross-section of  $5 \times 5$  and  $7.5 \times 7.5 \mu\text{m}^2$  with an assumed  $\frac{a_0}{W}$  ratio of 0.5, the initial ligament length is 2.5 and  $3.75 \mu\text{m}$ , whereby the neutral axis is close to the ligament halve. Thus, for these RT cantilevers the plastic zone size approaches the neutral axis. Therefore, compressive stresses may start to inhibit the plastic zone expansion. Hence, the energy dissipation from the crack tip is reduced, and fracture occurs at lower  $J_q$  and  $\delta$  values. Similar observations were reported by Wurmshuber et al.<sup>33</sup> for cantilevers with a cross-section of  $3 \times 3 \mu\text{m}^2$  made from grain boundary-doped tungsten alloys with a grain size of about 150 nm.

From the 400 °C sample, cantilevers with a cross-section of  $5 \times 5$  and  $10 \times 10 \mu\text{m}^2$  were fabricated to reduce FIB time, as the RT cantilevers with a cross-section of  $10 \times 10 \mu\text{m}^2$  confirmed size independency already. Fracture mechanical evaluation for the 400 °C sample revealed a  $J_q$  of  $230 \pm 40$  and  $210 \pm 60 \frac{\text{J}}{\text{m}^2}$  for the  $5 \times 5$  and  $10 \times 10 \mu\text{m}^2$  cantilever cross-sections; see Fig. 10a. Combined with the yield strength estimated from the hardness values, this gives a pre-factor  $C$  of 66 for the  $10 \times 10 \mu\text{m}^2$  cantilevers, which is well above the size dependency range of 10 to 50 given in the literature.<sup>24,27,29,31–33</sup> The cantilevers with a cross-section of  $5 \times 5 \mu\text{m}^2$  exhibit a pre-factor value of 35, which is within a similar range as the  $10 \times 10 \mu\text{m}^2$  cantilevers fabricated from the RT sample; see Fig. 9. Despite the cross-sectional difference, the mechanical data of the 400 °C cantilevers showed no size-dependent trend. Nevertheless,  $\delta$  was measured from in situ images, revealing a  $\delta$  of  $90 \pm 6$  and  $91 \pm 6$  nm for the 400 °C cantilevers, illustrated in Fig. 10b. Transforming the  $\delta$  into  $J_{q,\delta}$  gives  $230 \pm 20$  and  $240 \pm 20 \frac{\text{J}}{\text{m}^2}$  for the  $5 \times 5$  and  $10 \times 10 \mu\text{m}^2$  cantilevers, which are in accordance with the  $J_q$  determined. The plane strain condition for the 400 °C cantilevers was verified by Eq. 4, which gives a minimal size constrain of  $1.2 \mu\text{m}$ , as met by all 400 °C cantilevers. Furthermore, the

plastic zone size was estimated according to Eq. 5 as  $0.7 \pm 0.2 \mu\text{m}$ , which fits well into a quarter of the initial ligament length of the  $5 \times 5 \mu\text{m}^2$  cantilevers. Therefore, compressive stresses below the neutral axis do not interfere with the plastic zone. Nevertheless, the fracture behavior differs for the 400 °C cantilever between  $5 \times 5$  and  $10 \times 10 \mu\text{m}^2$ , as the former fractured by stable crack growth while the latter exhibits unstable failure. This change in fracture behavior might originate from the fact that with decreasing size less energy is stored in the sample, stabilizing crack propagation through reduced energy release capabilities. This behavior is also reflected in the increasing tearing modulus by decreasing the sample size; see Fig. 8 and Ref. 30. Hence, stable crack growth might occur because of the size reduction, whereby displacement controlled quasi-static loading might be further beneficial for a stable crack growth, as during unloading elastically stored energy is released and has to be reapplied during the following loading segment. Despite the size-dependent crack propagation, the crack initiation is size independent as long as Eq. 4 is fulfilled.<sup>42</sup>

Comparing the RT and 400 °C sample microstructure suggests that the nanocomposite matrix grain size, increasing from 9 to 28 nm, has only a minor impact on  $J_q$ , although larger grains could potentially accumulate more dislocations. In contrast, the coarse tungsten grains present in the nanocrystalline matrix have a significant effect on  $J_q$  and  $J_{q,\delta}$ . In the RT samples, these coarse tungsten grains form delamination-like structures, lowering the stress triaxiality and leading to an anisotropic fracture behavior. From an engineering point of view, while this anisotropic characteristic could be harnessed in dedicated component design, isotropic material properties are favorable regarding ease of material use and safety regarding unintended loading situations. For the cantilevers deformed at elevated temperatures, the spherically shaped coarse tungsten grains led to an isotropic microstructure and connected material properties. Nevertheless, cantilevers fabricated from the RT sample exhibited a high  $J_q$  and  $J_{q,\delta}$  of about  $410 \frac{\text{J}}{\text{m}^2}$ , while only  $220 \frac{\text{J}}{\text{m}^2}$  were obtained from the 400 °C cantilevers.

To further underline the attractive properties of the present material, the metric proposed by Hohenwater et al.<sup>45</sup> for damage tolerance was used to classify the results regarding literature data for grain refined copper, tungsten and tungsten-copper composites. This metric is given by the product of  $K_{IC}$  and the material strength; as for damage tolerance, a one-dimensional viewpoint is insufficient. A damage tolerant material must combine a high material strength, as this defines the onset of plastification, and a high fracture toughness, which is a measure for the crack growth resistance. The iso-lines in Fig. 11 illustrate this respective damage

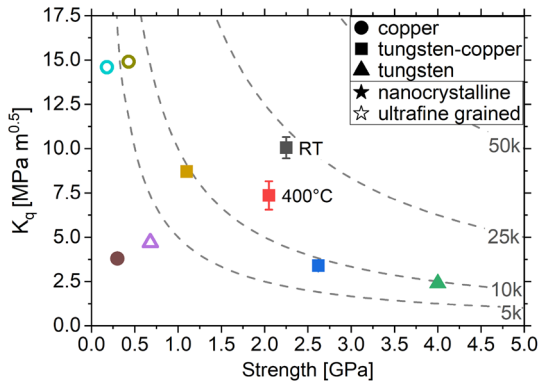


Fig. 11. Relation of the investigated composite to refined material compositions, ultra-fine grained copper (cyan circle),<sup>51</sup> nanotwined copper (olive circle),<sup>50</sup> nanocrystalline copper<sup>46</sup> (brown dot), nanocrystalline tungsten-copper with 75 at.% copper (orange rectangle),<sup>52</sup> ultra-fine grained tungsten (unfilled purple triangle),<sup>48</sup> nanocrystalline tungsten-copper with 50 at.% copper (blue rectangle)<sup>49</sup> and magnetron sputtered tungsten (green triangle)<sup>47</sup> (Color figure online).

tolerance. The investigated tungsten-copper composite showcases a noticeably increased fracture toughness compared to other nanostructured materials such as nanocrystalline copper,<sup>46</sup> nanocrystalline magnetron sputtered tungsten,<sup>47</sup> polycrystalline tungsten<sup>48</sup> and a nanocrystalline tungsten-copper composite with 50 at.% copper.<sup>49</sup> The latter has a comparable composition and similar grain size of 10 nm as the here-investigated RT sample. Comparing the fracture toughness reveals an increased value for the present RT sample, which stems from the coarse flake-like tungsten grains, transforming the stress state. For the 400 °C specimen, the coarse tungsten grains were spherically shaped, and the grain size increased to 27 nm. Due to the spherical shape the coarse tungsten grains have reduced influence on the fracture toughness. Nevertheless, the 400 °C specimen exhibits an increased fracture toughness compared to the tungsten-copper composite with 50 at.% copper<sup>49</sup> reported in literature. This fracture toughness increase can be attributed to the increased grain size. A similar trend can be deduced from the nanocrystalline<sup>46</sup> and ultrafine-grained<sup>50,51</sup> copper. The tungsten-copper composite with 75 at.%<sup>52</sup> has a similar fracture toughness level to the investigated composites, as the additional amount of copper enhanced the ductility. However, the strength is only in the range of 1 GPa and thus well below the present material. Consequently, the damage tolerance also increased from 10.000 MPa  $\sqrt{m}$ , where the nanocrystalline tungsten and tungsten-copper composites reside, to 25.000 MPa  $\sqrt{m}$  for the present case; see the iso-lines in Fig. 11. However, due to the observed intercrystalline fracture, the damage tolerance of the tungsten-copper composite would benefit from grain boundary strengthening, e.g.,

by grain boundary segregation.<sup>52</sup> Another possibility to enhance the damage tolerance would be to strengthen the copper phase and enable twinning as an additional deformation mechanism, e.g., by alloying copper with zinc.<sup>53</sup>

Motivated by the promising material properties of this microstructurally optimized tough nanocomposite, possibilities for transferring the achieved results to a large-scale production become of interest. One possibility would be to sinter bulk materials of nanocrystalline powders by liquid phase sintering or field-assisted flash sintering. However, processing of nanocrystalline powder is challenging because of oxidation, the necessity to remove powder agglomerates and the unwanted contamination of the powder with elements from the grinding balls or vial. Furthermore, direct upscaling of HPT is limited to thickness of 10 mm and diameter of  $\varnothing 60$  mm because of the required pressure.<sup>54</sup> Nevertheless, different severe plastic deformation methods are available in the literature for continuous or quasi-continuous material synthesis, e.g., accumulative roll bonding (ARB),<sup>55,56</sup> equal channel angular pressing (ECAP),<sup>57</sup> incremental high-pressure torsion (I-HPT),<sup>58</sup> continuous high-pressure torsion (C-HPT)<sup>54</sup> and high pressure tube twisting (HPTT).<sup>59,60</sup> However, these techniques often lack the achievable high strain that can be conveniently imposed by HPT. ARB necessitates sintered material sheets as basis and stacks material sheets to bind them by rolling. During stacking, different material components like particles, fibers, or foils can be incorporated to enhance the material properties.<sup>55</sup> Nevertheless, ARB results in a layered structure with anisotropic material properties. For the application of C-HPT, HPTT and I-HPT, a sintered base material is required, and the processing will result again in a textured microstructure.<sup>60</sup> However, similarly to the present results, application of an increased deformation temperature could reduce the microstructural texture for these techniques. Last, ECAP allows to directly consolidate powders, which produces a significant compositional design and produces an isotropic microstructure when following appropriate billed pressing paths. Hence, ECAP might be a promising candidate to upscale fabrication of nanocrystalline immiscible nanocomposite materials.

## CONCLUSION

A bulk tungsten-copper composite was subjected to high-pressure torsion at different deformation temperatures to tailor the grain size into the nanocrystalline regime, resulting in a bi-modal microstructure despite refinement saturation. By raising the deformation temperature from room temperature to 400 °C, the matrix grain size was increased by a factor of three from 9 to 28 nm, whereby coarse tungsten grains embedded in the nanocrystalline matrix changed from a flake-like

shape to spherical and enlarged in size. Micro-cantilever bending beams with varying size were fabricated to study a possible size effect and the impact of the matrix grain size, utilizing elastic-plastic fracture mechanical evaluation and in situ images from the crack initiation point. Inter-crystalline fracture governs the failure process, with features roughly corresponding to the matrix grain size. Additionally, for room temperature cantilevers, the coarse flat tungsten grains formed delamination-like structures on the fracture surface, which reduced the stress triaxiality at the crack front and therefore increased the fracture toughness. Furthermore, the room temperature cantilevers failed mainly by stable crack growth and revealed a size dependency below a cantilever cross-section of  $10 \times 10 \mu\text{m}^2$  as then the plastic zone size approached the neutral axis. For 400 °C cantilevers, no delaminations formed on the fracture surface, as the crack path passed the spherical coarse tungsten grains. Nevertheless, the fracture behavior changed from unstable to stable with decreasing cantilever cross-section. This occurs as with reduced sample volume less energy is stored in the cantilever, as reflected in the size dependency of the tearing modulus. Despite the different fracture behavior, the determined characteristics are similar, as the criteria for size independent crack initiation values are met. The matrix grain size had only a marginal influence on the fracture characteristics, while the delamination-like structures formed by the coarse flat tungsten grains significantly increased the fracture toughness. This further allows to tailor the material transition from a tungsten shield to the copper cooling block.

#### ACKNOWLEDGMENTS

This work was supported by European Research Council [Grant Number: 771146 (TOUGHIT)]. We thank Christina Kainz for the nanoindentation measurements.

#### FUNDING

Open access funding provided by Montanuniversität Leoben.

#### AVAILABILITY OF DATA AND MATERIALS

The data generated during the current study are available from the corresponding author on a reasonable request.

#### CONFLICT OF INTEREST

The authors declare that they have no conflict of interest.

#### OPEN ACCESS

This article is licensed under a Creative Commons Attribution 4.0 International License, which permits use, sharing, adaptation, distribution and reproduction in any medium or format, as long as

you give appropriate credit to the original author(s) and the source, provide a link to the Creative Commons licence, and indicate if changes were made. The images or other third party material in this article are included in the article's Creative Commons licence, unless indicated otherwise in a credit line to the material. If material is not included in the article's Creative Commons licence and your intended use is not permitted by statutory regulation or exceeds the permitted use, you will need to obtain permission directly from the copyright holder. To view a copy of this licence, visit <http://creativecommons.org/licenses/by/4.0/>.

#### REFERENCES

1. J.W. Davis, V.R. Barabash, A. Makhankov, L. Plöchl, and K.T. Slattery, *J. Nucl. Mater.* 258–263, 308 [https://doi.org/10.1016/S0022-3115\(98\)00285-2](https://doi.org/10.1016/S0022-3115(98)00285-2) (1998).
2. Y. Ueda, K. Tobita, and Y. Katoh, *J. Nucl. Mater.* 313–316, 32 [https://doi.org/10.1016/S0022-3115\(02\)01329-6](https://doi.org/10.1016/S0022-3115(02)01329-6) (2003).
3. M. Rieth, D. Armstrong, B. Dafferner, S. Heger, A. Hoffmann, M.D. Hoffmann, U. Jäntsch, C. Kübel, E. Materna-Morris, J. Reiser, M. Rohde, T. Scherer, V. Widak, H. Zimmermann, *5th FORUM NEW Mater. PART B.* 73 (211AD) 11. <https://doi.org/10.4028/www.scientific.net/as-t.73.11>.
4. D. Sun, Y. Wang, S. Huang, J. Zhao, G. Liu, and J. Li, *Fusion Eng. Des.* 120, 9 <https://doi.org/10.1016/j.fusengdes.2017.05.006> (2017).
5. E. Tejado, A.V. Müller, J.H. You, and J.Y. Pastor, *Mater. Sci. Eng. A* 712, 738 <https://doi.org/10.1016/j.msea.2017.12.054> (2018).
6. X. Chen, W. Sun, X. Li, X. Wang, H. Yan, and K. Li, *Fusion Eng. Des.* 137, 349 <https://doi.org/10.1016/j.fusengdes.2018.10.016> (2018).
7. International Atomic Energy Agency, Technical Basis for the Iter Final Design Report, Cost Review and Safety Analysis, Int. Organ. (1998).
8. E. Gaganidze, D. Rupp, and J. Aktaa, *J. Nucl. Mater.* 446, 240 <https://doi.org/10.1016/j.jnucmat.2013.11.001> (2014).
9. V. Barabash, A. Peacock, S. Fabritsiev, G. Kalinin, S. Zinkle, A. Rowcliffe, J.W. Rensman, A.A. Tavassoli, P. Marmy, P.J. Karditsas, F. Gillemot, M. Akiba, *J. Nucl. Mater.* 367-370 A (2007) 21. <https://doi.org/10.1016/j.jnucmat.2007.03.017>.
10. S.J. Park, Y.S. Kwon, S. Lee, J.L. Johnson, R.M. German, *Proc. World Powder Metall. Congr. Exhib. World PM 2010.* 5 (2010) 2010.
11. E. Tejado, A.V. Müller, J.H. You, and J.Y. Pastor, *J. Nucl. Mater.* 498, 468 <https://doi.org/10.1016/j.jnucmat.2017.08.020> (2018).
12. A. Khalajhedayati, Z. Pan, and T.J. Rupert, *Nat. Commun.* <https://doi.org/10.1038/ncomms10802> (2016).
13. M. Wurmshuber, S. Dopfermann, S. Wurster, S. Jakob, M. Balooch, M. Alfreider, K. Schmuck, R. Bodlos, L. Rومانer, P. Hosemann, H. Clemens, V. Maier-Kiener, and D. Kiener, *Int. J. Refract. Met. Hard Mater.* 111, 106125 <https://doi.org/10.1016/j.ijrmhm.2023.106125> (2023).
14. R.W. Armstrong, *Mater. Trans.* 55, 2 <https://doi.org/10.2320/matertrans.MA201302> (2014).
15. E.O. Hall, *Proc. Phys. Soc. Sect. B* 64, 747 <https://doi.org/10.1088/0370-1301/64/9/303> (1951).
16. N. Petch, *J. Iron. Steel Res. Int.* 174, 25 (1953).
17. I. Sabirov, and R. Pippan, *Scr. Mater.* 52, 1293 <https://doi.org/10.1016/j.scriptamat.2005.02.017> (2005).
18. K.S. Kormout, R. Pippan, and A. Bachmaier, *Adv. Eng. Mater.* 19, 1 <https://doi.org/10.1002/adem.201600675> (2017).
19. M. Burtscher, M. Zhao, J. Kappacher, A. Leitner, M. Wurmshuber, M. Pfeifenberger, V. Maier-Kiener, and D. Kiener, *Nanomaterials* 11, 1 <https://doi.org/10.3390/nano11112951> (2021).

20. M. Burtscher, M. Alfreider, C. Kainz, K. Schmuck, and D. Kiener, *Mater. Des.* 220, 110848 <https://doi.org/10.1016/j.matdes.2022.110848> (2022).
21. R. Pippan, S. Scheriau, A. Hohenwarter, and M. Hafok, *Mater. Sci. Forum.* 584–586, 16 (2008).
22. R. Achanta, A. Shaji, K. Smith, A. Lucchi, P. Fua, and S. Süssstrunk, *IEEE Trans. Pattern Anal. Mach. Intell.* 34, 2274 (2012).
23. M.J. Pfeifenberger, M. Mangang, S. Wurster, J. Reiser, A. Hohenwarter, W. Pfleging, D. Kiener, and R. Pippan, *Mater. Des.* 121, 109 <https://doi.org/10.1016/j.matdes.2017.02.012> (2017).
24. S. Wurster, C. Motz, and R. Pippan, *Philos. Mag.* 92, 1803 <https://doi.org/10.1080/14786435.2012.658449> (2012).
25. M. Alfreider, S. Kolitsch, S. Wurster, and D. Kiener, *Mater. Des.* 194, 3 <https://doi.org/10.1016/j.matdes.2020.108914> (2020).
26. M. Alfreider, D. Kozic, O. Kolednik, and D. Kiener, *Mater. Des.* 148, 177 <https://doi.org/10.1016/j.matdes.2018.03.051> (2018).
27. ASTM Standard E1820, Standard Test Method for Measurement of Fracture Toughness, ASTM B. Stand. (2013). <https://doi.org/10.1520/E1820-13>.
28. H. Ledbetter, and S. Datta, *JSME* 34(2), 194 (1991).
29. C.F. Shih, and M.D. German, *Int. J. Fract.* 17, 27 <https://doi.org/10.1007/BF00043119> (1981).
30. A.G. Atkins, Z. Chen, and B. Cotterell, *Proc. R. Soc. A Math. Phys. Eng. Sci.* 454, 815 (1998).
31. J. Ast, M. Ghidelli, K. Durst, M. Göken, M. Sebastiani, and A.M. Korsunsky, *Mater. Des.* 173, 107762 <https://doi.org/10.1016/j.matdes.2019.107762> (2019).
32. X.K. Zhu and J.A. Joyce, *Eng. Fract. Mech.* 85, 1 <https://doi.org/10.1016/j.engfracmech.2012.02.001> (2012).
33. M. Wurmshuber, M. Alfreider, S. Wurster, R. Pippan, and D. Kiener, *Acta Mater.* 250, 18 <https://doi.org/10.1016/j.actamat.2023.118878> (2022).
34. P. Zhang, S.X. Li, and Z.F. Zhang, *Mater. Sci. Eng. A* 529, 62 <https://doi.org/10.1016/j.msea.2011.08.061> (2011).
35. C.E. Carlton, and P.J. Ferreira, *Acta Mater.* 55, 3749 <https://doi.org/10.1016/j.actamat.2007.02.021> (2007).
36. S.N. Naik and S.M. Walley, *J. Mater. Sci.* 55, 2661 <https://doi.org/10.1007/s10853-019-04160-w> (2020).
37. M. Spittel and T. Spittel, *Berlin*. <https://doi.org/10.1007/978-3-642-14174-4> (2016).
38. L. Schweiger, D. Kiener, M. Burtscher, E. Schafner, G. Mori, F. Spieckermann, and J. Eckert, *Mater. Today Adv.* 20, 100433 <https://doi.org/10.1016/j.mtaadv.2023.100433> (2023).
39. R. Hertzberg, R. Vinici, and J. Hertzberg, *Deformation and Fracture Mechanics of Engineering Materials*, 5th edn. (Wiley, Hoboken, NJ, 1985).
40. A. Hohenwarter, C. Kammerhofer, and R. Pippan, *J. Mater. Sci.* 45, 4805 <https://doi.org/10.1007/s10853-010-4635-9> (2010).
41. O. Kolednik, M. Sistaninia, and S. Kolitsch, *Eng. Fract. Mech.* <https://doi.org/10.1016/j.engfracmech.2023.109636> (2023).
42. R. Pippan, S. Wurster, and D. Kiener, *Mater. Des.* 159, 252 <https://doi.org/10.1016/j.matdes.2018.09.004> (2018).
43. T.L. Anderson, *Fracture Mechanics*, 3rd edn. (CRC Press, Boca Raton, 2005).
44. R. Irwin, George, *Fracture dynamics*, *Fract. Met.* (1947). <https://cir.nii.ac.jp/crid/1573950400137757952.bib?lang=en>. Accessed April 25, 2023.
45. A. Hohenwarter, R. Pippan, *Philos. Trans. R. Soc. A Math. Phys. Eng. Sci.* (2015) <https://doi.org/10.1098/rsta.2014.0366>.
46. R.R. Keller, J.M. Phelps, and D.T. Read, *Mater. Sci. Eng. A* 214, 42 [https://doi.org/10.1016/0921-5093\(96\)10253-7](https://doi.org/10.1016/0921-5093(96)10253-7) (1996).
47. E. Harry, A. Rouzaud, P. Juliet, Y. Pauleau, and M. Ignat, *Surf. Coatings Technol.* 116–119, 172 [https://doi.org/10.1016/S0257-8972\(99\)00071-7](https://doi.org/10.1016/S0257-8972(99)00071-7) (1999).
48. B. Gludovatz, S. Wurster, A. Hoffmann, R. Pippan, *12th Int. Conf. Fract.* 2009, ICF-12. 7 (2009) 5365. <https://doi.org/10.1016/j.ijrmhm.2010.04.007>.
49. M. Burtscher, M. Alfreider, C. Kainz, and D. Kiener, *Mater. Sci. Eng. A* 887, 145760 <https://doi.org/10.1016/j.msea.2023.145760> (2023).
50. A. Singh, L. Tang, M. Dao, L. Lu, and S. Suresh, *Acta Mater.* 59, 2437 <https://doi.org/10.1016/j.actamat.2010.12.043> (2011).
51. D. Rahmatabadi, M. Tayyebi, A. Sheikhi, and R. Hashemi, *Mater. Sci. Eng. A* 734, 427 <https://doi.org/10.1016/j.msea.2018.08.017> (2018).
52. M. Wurmshuber, M. Burtscher, S. Dopfermann, R. Bodlos, D. Scheiber, L. Romaner, and D. Kiener, *Mater. Sci. Eng. A* 857, 144102 <https://doi.org/10.1016/j.msea.2022.144102>.
53. Y.H. Zhao, X.Z. Liao, Y.T. Zhu, Z. Horita, and T.G. Langdon, *Mater. Sci. Eng. A* 410–411, 188 <https://doi.org/10.1016/j.msea.2005.08.074> (2005).
54. Z. Horita, Y. Tang, T. Masuda, and Y. Takizawa, *Nippon Kinzoku Gakkaishi/Journal Japan Inst. Met.* 86, 107 <https://doi.org/10.2320/JINSTMET.J2022009> (2022).
55. T. Hausöl, V. Maier, C.W. Schmidt, M. Winkler, H.W. Höppel, and M. Göken, *Adv. Eng. Mater.* 12, 740 <https://doi.org/10.1002/adem.201000044> (2010).
56. M. Ebrahimi, and Q. Wang, *J. Mater. Res. Technol.* 19, 4381 <https://doi.org/10.1016/j.jmrt.2022.06.175> (2022).
57. K. Matsuki, T. Aida, T. Takeuchi, J. Kusui, and K. Yokoe, *Acta Mater.* 48, 2625 [https://doi.org/10.1016/S1359-6454\(00\)00061-6](https://doi.org/10.1016/S1359-6454(00)00061-6) (2000).
58. A. Hohenwarter, *Mater. Sci. Eng. A* 626, 80 <https://doi.org/10.1016/j.msea.2014.12.041> (2015).
59. L.S. Toth, C. Chen, A. Pougis, M. Arzaghi, J.J. Fundenberger, R. Massion, S. Suwas, *Mater. Trans.* 60, 1177 <https://doi.org/10.2320/matertrans.MF201910> (2019).
60. M. Arzaghi, J.J. Fundenberger, L.S. Toth, R. Arruffat, L. Faure, B. Beausir, X. Sauvage, *Acta Mater.* 60, 4393 <https://doi.org/10.1016/j.actamat.2012.04.035> (2012).

**Publisher's Note** Springer Nature remains neutral with regard to jurisdictional claims in published maps and institutional affiliations.